Characterisation of shallow overpressure in consolidating submarine slopes via seismic full waveform inversion

Giuseppe Provenzano[1], Antonis Zervos[2], Mark E. Vardy[3], Timothy J. Henstock[4]

10/14/2019

Abstract: Pore pressures higher than hydrostatic correspond to localised reductions of the level of stress required to induce lateral mass movement in a slope, and therefore play a key role in preconditioning submarine landsliding. In this paper, we investigate whether multi-channel seismic reflection data can be used to infer potentially destabilising pore-pressure levels at a resolution and sensitivity useful for in-situ slope stability characterisation. We simulate the continuous deposition of sediment on consolidating slopes in two scenarios, with combinations of sedimentation rate and permeability distribution leading to disequilibrium compaction. Ultra-high-frequency (*UHF*; 0.2-2.5 kHz) seismic reflection data are computed for each model and a stochastic full waveform inversion (*FWI*) method is used to retrieve the sub-seabed properties

Ocean and Earth Science, National Oceanography Centre Southampton, University of Southampton, European Way, Southampton UK, SO14 3ZH

Faculty of Engineering and the Environment, University of Southampton, Highfield, Southampton UK. SO17 1BJ

SAND Geophysics Limited,44 Chatsworth Road, Southampton UK, SO19 7NJ

Ocean and Earth Science, National Oceanography Centre Southampton, University of Southampton, European Way, Southampton UK, SO14 3ZH

from the computed seismograms. These are then interpreted as time-depth variations in the effective stress (σ') regime, and therefore local overpressure ratio and factor of safety, using a combination of p-wave velocity to σ' transforms. The results demonstrate that multi-channel UHF seismic data can provide valuable constraints on the physical properties distribution in the top 50 m below seabed at a sub-metric scale, and with a sensitivity useful to infer destabilising excess pore pressure levels.

Submarine landslides involve the movement of large sediment volumes, from tens of m^3 up to thousands km^3 (Halflidason et al., 2005; Masson et al., 2006; Madhusudhan et al., 2017), and occur in a variety of depositional environments (Garzaglia et al., 2005; Dugan & Sheahan, 2012; Shanmugam, 2015). Unlike their terrestrial equivalents, they are observed on very low-angle slopes (even below 2°) with relatively low sedimentation rates (e.g., Dugan & Flemings, 2000; Urlaub et al., 2012). Hazards associated with submarine landslides include human fatalities in near-shore settlements, damage to shoreline and/or offshore engineering structures (Masson et al., 2006; Shanmugam, 2015), and have the potential to extend to larger areas by inducing tsunamis travelling distances from 10s (Skvortsov & Bornhold, 2007; Conway et al., 2012) to 100s *km* (Halflidason et al., 2005).

Localised development of pore overpressure, i.e. pore pressure higher than hydrostatic, is commonly regarded as one of the most important preconditioning factors in the occurrence of slope failure (Leynaud et al., 2007; Flemings et al., 2008; Dugan & Sheahan, 2012). Abnormally pressured sediment beds are thought to act as glide planes of translational slides in both continental shelf and near-shore contexts (L'Heureux et al., 2012; Madhusudhan et al., 2017), and favour the occurrence of slope failure in the presence of transient loading caused by either natural causes, such as earthquakes or gas-hydrate dissociation (Stigall & Dugan, 2010), or anthropogenic, e.g. industrial blasting or piling (Masson et al., 2006; Vanneste et al., 2015).

Characterisation of the in-situ pore pressure of a shallow submarine slope traditionally relies on cores, boreholes and core penetrometers (*CPTs*; Steiner et al., 2012), which provide centimetre-to-millimetre vertical resolution data, but are logistically limited to a coarse spatial coverage. Unlike basin scale research (Marin-Moreno et al., 2012, 2013), non-invasive estimations of pore-pressure distribution are not commonly employed in offshore geotechnics, and, with few exceptions (e.g., Vardy, 2015), very rarely use the quantitative interpretation of geophysical data to infer in-situ stability conditions.

In this paper, we explore the potential of ultra-high-frequency (*UHF*; 0.2-4.0 kHz), decimetre-resolution, marine seismic reflection data for the remote detection and quantification of disequilibrium compaction. We simulate multi-channel seismic acquisition during the deposition of two synthetic submarine slopes, and use a stochastic FWI algorithm to reconstruct the p-wave velocity (V_p) distributions from the seismograms at different time steps. These are then interpreted as time-depth variations in the effective stress (σ') regime, and therefore local overpressure ratio and factor of safety, using a combination of V_p to σ' transforms commonly employed in basin research (Marin-Moreno et al., 2013) and pre-drill geohazard estimation (e.g., Eaton, 1975; Bowers, 1995; Sayers et al., 2002). The results suggest that multi-channel seismic reflection data has the potential to identify and map the stratigraphic and spatial variability in over-pressure, and therefore better constrain the in-situ stability conditions of submarine slopes undergoing loading in shallow water environments.

1 Methods

1.1 Submarine slope modelling

To test the sensitivity of UHF seismic reflection data to evolving pore pressure conditions, we simulate the deposition of one-dimensional elastic submarine slopes (Gibson, 1958; Huang &

Griffiths, 2010). Two scenarios (M-1 and M-2) are considered, with permeability structures and sedimentation rates similar to those observed in areas prone to shallow (≤50 m) landsliding: M-1 simulates a slope with strong permeability contrasts and high sedimentation rate, as it can be observed in river delta enviornments (Flemings et al., 2008; Long et al., 2011); M-2 represents a high-latitude continental shelf deposition, with clayey-slity coarsening upward sedimentary sequences (Madhusudhan et al., 2017).

In our formulation, the model is assumed to be under hydrostatic pore pressure conditions when loading starts, and soil particles are deposited over time according to a time-varying sedimentation rate, designed to approximate realistic conditions of a dynamic sedimentary environment.. Due to the added load, the slope will consolidate, with transient vertical pore fluid flow dissipating the excess pore pressure generated (Gibson, 1958). The governing equation of the problem is a diffusion-generation equation for the unknown excess head, h (Appendix A), i.e. the excess pore pressure normalised to the unit weight of water (γ_w):

$$\frac{E'_0}{\gamma_w}\left(\frac{\partial k}{\partial z}\frac{\partial h}{\partial z}+k\frac{\partial^2 h}{\partial z^2}\right)+\frac{\cos^2\Theta}{\gamma_w}\alpha=\frac{\partial h}{\partial t} \qquad (1)$$

where: z is the spatial coordinate and it's positive upwards; E'_0 is the one-dimensional stiffness; k is the kinematic permeability (m/s); Θ is the slope angle; α is the rate of increase of the vertical stress due to deposition. During deposition, the seafloor position, D, potentially changes as a result of the balance between deposition and settlement:

$$\frac{dD}{dt}=\frac{1}{\gamma_s}\alpha+k\left.\frac{\partial h}{\partial z}\right|_D \qquad (2)$$

where γ_s is the unit weight of the depositing sediment suspension. Therefore, the deposited sediments are not only accounted for as a load, but also included as a part of the aggrading and consolidating slope (Appendix B). The system of Eqs. 1 and 2 is solved with an implicit finite-

difference scheme in time and centred finite-difference in space (Ferziger & Perić, 2002). A zero-flow boundary condition at the bottom of the model ($\frac{\partial h}{\partial dz}$=0) simulates an impermeable bedrock, whereas the top of the model represents a free-draining surface (h=0).

Changes in the relationship between porosity (φ) and permeability (k), i.e in the coefficients of $k=c_1 e^{\varphi c_2}$ (e.g., Binh et al., 2009), are used to account for variations in sediment type within the model, simulating the effect of changing texture and pore-space connectivity (Pape et al., 1999). One-dimensional stiffness is assumed to be homogeneous and constant, representing soft, non-lithified sediments ($E'_0 \simeq 10^3 kPa$; e.g., Steiner et al., 2012). Solid grains are assumed incompressible, therefore load-induced deformations are entirely attributed to variations of the pore space volume, which leads to an evolving permeability distribution. Geometry and relative positions of impermeable bedrock, sediment and water for the two scenarios are presented in Fig. 1, together with qualitative vertical permeability profiles.

In parts of the sediment column where the transfer of the overburden load from the pore fluid to the solid skeleton is inhibited (*l-a* in Fig. 1), pore pressures higher than hydrostatic develop and the effective stress distribution deviates from equilibrium. As a result, the shear stress necessary to trigger failure is reduced (Gibson, 1958). To monitor this, for each time step, at each depth, the factor of safety (*FoS*) of the slope can be computed as the ratio between the available shear strength and the mobilised shear strength (Powrie, 2002, p. 502). This can be expressed in terms of the excess head:

$$FoS(z_i,t)=\frac{\tan\varphi'_{crit}}{\tan\Theta}\left[1-\frac{\gamma_w h}{z_i - \int_D (\gamma(z)-\gamma_w)dz\cos\Theta}\right] \quad (3)$$

where: $\gamma(z)$ is the bulk unit weight at depth z; Θ is the angle between the slope and the horizontal; and φ'_{crit} is its the friction angle. For a given Θ and φ'_{crit}, *FoS* lower than 1

correspond to slope failure. In these examples, the initial hydrostatic conditions, combined with φ_{crit}=12° and Θ=3°, correspond to a factor of safety $FoS \simeq 4$ (Eq. 3), i.e an initially very stable slope.

Another quantity that can be useful to monitor the effective stress condition of the slope is the *overpressure ratio* (λ^*), defined at each depth as the ratio between the excess pore pressure, p_e, and the effective stress in hydrostatic conditions:

$$\lambda^* = \frac{p_e}{\sigma - p_h} \tag{4}$$

where σ is the lithostatic stress, obtained by depth-integrating γ(z), and p_h is the hydrostatic pore pressure. When under hydrostatic conditions (i.e. at t=0), λ^* is zero; when the effective stress is zero and, therefore, the sediments have no shear strength left (Powrie, 2002), it reaches one. Since the denominator of Eq. 4 is null at the seafloor (Powrie, 2002), a taper is applied to λ^* in the top 2 m of the model, in order to avoid numerical instability.

1.2 Seismic characterisation

1.2.1 Forward modelling

For each of these burial models, the acquisition of multi-channel marine seismic reflection data has been simulated at four selected time steps corresponding to significant changes in effective stress conditions. In order to do so, for each time step, a p-wave velocity (V_p) model is estimated from the the slope model output.

During consolidation, relative volumetric changes of pore-space and solid grains modify the response of the multi-phase medium to mechanical wave propagation (e.g., Mavko et al., 2009). For non-lithified sediments, this is of greater extent than, for instance, the lithology of the solid

grains (e.g., Vardy et al., 2017). In the absence of fluid-substitution and thermo-chemical effects, it is therefore sensible to use porosity (φ) as the parameter most directly affecting the acoustic properties of the subsurface. An under-compaction anomaly produces a localised reduction in seismic wave velocity and, if this is within the seismic resolution, it has a footprint on the seismic data (e.g. Mallick & Dutta, 2002; Marin-Moreno et al., 2013) in terms of reflection amplitude and/or traveltime. In order to simulate such physical dependency of V_p from φ, we use a quadratic relationship derived from in-situ measurements of shallow sediment properties in a variety of depositional environments (Vardy, 2015).

For each time step, the propagation of an ultra-high-frequency wavefield is simulated within the derived V_p models using an isotropic, acoustic reflectivity modelling scheme for a layered half space (Schmidt & Jensen, 1985). In the simulation, a minimum phase impulsive acoustic source (Verbeek & McGee, 1995), with a bandwidth spanning $0.2-2.5kHz$, is combined with a surface-towed 60-m long array of receivers with 1-m spacing. This acquisition design is representative of a typical 2D multi-channel UHF seismic reflection survey (e.g. Pinson, 2009; Duarte et al., 2017; Monrigal et al., 2017). Such surveys propagate and record effectively dominant wavelengths in the order of 1 m in slow sediments (V_p=$1.5-1.7km/s$), and have therefore a resolution sufficient to image metric to sub-metric scale anomalies (Sheriff & Geldart, 1995) potentially leading to slope destabilisation.

1.2.2 Inverse modelling

The synthetic seismic data generated from the slope models are then inverted for the p-wave velocity distribution within the slope, as if they were acquired in the field, and the model properties were unknown. In doing so, we simulate the application of geophysical data for the estimation of the subsurface properties, where the only known data is the recorded seismic wavefield (hereafter referred to as synthetic field data), and the propagation medium is reconstructed through an inversion process. Seismic inversion is here performed using a *genetic*

algorithm (GA; Goldberg, 1989), as presented in Provenzano et al. (2018), and summarised in Fig.2.

Starting from a p-wave velocity trend, obtained via analysis of the reflections' traveltime (Sheriff & Geldart), the inversion obtains a higher-resolution Vp model by iteratively fitting the reflections' full waveform, i.e. the entire recorded seismogram. An initial population of random p-wave models is generated by perturbing the starting profile within a range of plausible solutions. For each model a seismic dataset is computed, using the same forward modelling scheme employed to compute the synthetic field data, and assuming the source wavelet is known. In real cases, the latter can be estimated from the data (e.g. Ulrych, 1971; Dey & Lines, 1998), or deconvolved using a source-normalised scheme (Lee & Kim, 2003; Provenzano et al., 2017). The performance, or fitness, of each model is evaluated as the reciprocal of the L1-residual between the input seismic waveform and the inverted one, regularised so that smooth models are privileged over rough ones (Menke, 1989). All models with fitness better than average, together with individuals randomly selected among the entire ensemble, are designated to survive and propagate their characteristics to the following generation, through cross-over and random mutation. This process iteratively increases the average performance of the model ensemble, until the input full waveform is reconstructed within a desired confidence. Multiple runs are performed, each starting from an independent random population of models, thereby producing an ensemble of statistically independent solutions, from which a robust median model and confidence intervals can be computed (Sen & Stoffa, 1996; Vardy, 2015).

1.3 Estimation of effective stress conditions

The solution of the seismic inverse problem can be interpreted in terms of effective stress (σ') conditions using a number of empirical relationships (e.g., Sayers et al., 2002). Empirical methods assume that Vp in a granual water-saturated medium increases solely as a function of vertical effective stress (Marin-Moreno et al., 2013). Namely, p-waves propagates faster as the

porosity decreases and grain contact increases, and any reduction of Vp is attributed to disequilibrium compaction. Under this assumption, Vp can be used as a proxy to effective stress, and therefore, excess pore pressure and *FoS* within the slope.

Here we combine different methods commonplace in marine geohazard analysis (Sayers, 2006) in order to derive effective stress from V_p:

1. Bowers (1995). It assumes a relationship of the kind $V_p=V_0+A\sigma'^B$, where V_0 is the p-wave velocity of the saturated sediment at zero effective stress (taken to be V_p at the seafloor), and A,B are constants that require site-specific calibration. Effective stress can then be estimated as $\sigma'=[(V_p-V_0)/A]^{1/B}$. This method, developed on sonic velocity well-log data, is in principle capable of accounting for effective stress reductions due to factors other than disequilibrium compation, such as thermal fluid expansion (Bowers, 1995).

2. Eaton (1975). It is based on the equation $\sigma'=(\sigma_z-p_h)(V_p/V_h)^{k_e}$, where V_h is the p-wave velocity under hydrostatic conditions, and k_e is the *Eaton* exponent, controlling the sensitivity of the estimated σ' to V_p anomalies. Here the equilibrium V_h is extrapolated by using a log-linear relationship (e.g., Sayers et al., 2002), calibrated on a normally pressured portion of the model. This method is widely applied in the oil and gas industry, and it is appropriate when undercompaction is the main source of excess pore pressure (Bowers, 1995).

3. Westbrook (1991) equivalent depth method, as implemented by Marin-Moreno et al. (2013). In equilibrium, p-wave velocity increases with burial depth as a consequence of the increased effective stress and grain contact. If under-compaction occurs, velocity approaches values that would be observed at a shallower depth under hydrostatic conditions. Specifically, $V_p(z)$ observed at depth z within a under-compacted zone is

assumed to be equal, within a tolerance, to $V_p(z^*)$ at a shallower *equivalent* depth z^* in hydrostatic conditions, from which $\sigma'(z)=\sigma(z^*)-p_h(z^*)$.

Excess pore pressure can then be derived from the different effective stress estimates as $p_e(z)=\sigma(z)-p_h(z)-\sigma'(z)$, where $\sigma(z)$ is the lithostatic stress. The latter can be obtained by depth-integrating the estimated bulk unit weight, defined as $\gamma_{est}(z)=\gamma_g(1-\varphi_{est}(z))+\gamma_w\varphi_{est}(z)$, where porosity φ_{est} is derived from the inverted V_p using an appropriate $V_p-\varphi$ relationship (e.g., Richardson & Briggs, 1993), assumed to be known. Finally Eqs. 3- 4 are used for *FoS* and λ^*. In order to estimate the *FoS* (Eq. 3), the friction angle ($\varphi'_{crit}=12^\circ$) of the sediment and the slope angle ($\Theta=3^\circ$) must be known. The latter can be obtained from migrated seismic reflection images Sheriff & Geldart (1995), whereas φ_{crit} has no obvious footprint on the seismic data (Dugan & Sheahan, 2012), and should ideally be measured on soil samples.

The aforementioned combination of methods is applied to the solution V_p-model and its 95% confidence interval, in order to provide upper and lower limits of estimated pore pressure and, therefore worst- and best-case scenario predictions of slope stability conditions. By combining techniques derived independently and relying on different physical assumptions, we aim to provide insights about the uncertainties related to the remote estimation of overpressure.

2 Results

2.1 Synthetic slope models

The first scenario (M-1) models the fast deposition of a low-permeability layer within a high-permeability sedimentary column (Fig. 1 and Tab. 1). The high permeability contrast, replicating a sand-clay transition, and the high sedimentation rate, have been observed in delta

environments, such as the Ursa Basin in the Gulf of Mexico (Flemings et al., 2008; Long et al., 2011), associated with shallow seabed failure. The evolution of the slope properties is presented in Fig. 3a-d. When deposition starts, a 1-m thick layer of permeable sediment ($k \simeq 10^{-6} m/s$) sits in equilibrium above the impermeable bedrock. A sediment of the same type is deposited at a rate of 3*mm/yr*, until, after 800 years of modelled deposition, a 1-m-thick low kinematic permeability ($k \simeq 10^{-9} m/s$) layer is deposited at a faster rate (30*mm/yr*), before reverting to the previous deposition of permeable sediment at 3mm/yr. Failure is attained at the bottom of the lower-permeability layer 1.6 ka after simulation started.

The second scenario (M-2) consists of the deposition of a repeated coarsening upward, clayey-silty sedimentary sequence (Fig. 1 and Tab. 1). Such a structure is loosely based upon core-logs from the continental-shelf AFEN complex (Atlantic Frontier Environmental Network; Madhusudhan et al., 2017), which represents a typical high-latitude continental shelf deposition. Compared to model M-1, lower initial porosity (0.6 vs 0.7) and low overall permeability (10^{-9} m/s), associated with slow sedimentation, simulate the deposition of finer-grained sediments deposited in a more distal environment. Model characteristics are summarised in Table 1 and properties evolution is presented in Fig. 3e-h. Each sequence's top boundary, at 10 and 20 m below seafloor (m.b.s.f.), is marked by a sharp decrease in permeability, and sedimentation rate is constant. This produces a smooth λ^* profile, which corresponds to failure after 12.7 ka of modelled deposition at the deepest low-permeability bed.

2.2 Seismic characterisation

2.2.1 Forward modelling

In Fig. 4, the seismic traces recorded at the nearest offset (13 m source-receiver distance) are plotted as a function of two-way traveltime (twtt) at the same modelling time steps shown in Fig. 3. The traveltime of the seabed reflection decreases with time as a consequence of the

seafloor rising during deposition (Eq. 2). Similarly, the reflection originating at the sediment-bedrock interface also arrives at earlier traveltimes; a result of the increased velocities along the ray-path due to sediment deposition and consolidation. Sediment consolidation also has the effect of reducing the reflection coefficient at the lowermost interface. In M-1, this is apparent in a reduction of reflection strength; in M-2, at t-3, the acoustic impedance of the sediment becomes higher than the one of the bedrock (e.g., Sheriff & Geldart, 1995), as is revealed by the change of polarity of the bottom reflection.

The effect of disequilibrium compaction is apparent in M-1 as a negative polarity reflection at t-4 (0.047 s twtt), characterised by a change in the wavelet shape due to tuning within the overpressured layer. In M-2, under-compaction produces a reflection (0.065 s twtt) at t-3, whose strength increases until t-4, when failure is induced. Also in this case, the phase of the wavelet changes as a result of tuning occurring at the abrupt 20 m-deep velocity increments.

It is worth pointing out how similar values of λ^* correspond to significantly different reflection amplitudes, because the latter are dependent on porosity *contrasts* at model interfaces, rather than on the absolute overpressure level. Therefore, in the following two subsections, we will use FWI in order to estimate disequilibrium compaction from a quantitative simulation of the propagation phenomena within the evolving subsurface, including traveltime, amplitude and wavelet shape (e.g. Virieux & Operto, 2009).

2.2.2 Inverse modelling

Seismic inversion is applied at two time steps during deposition: t-2, corresponding to mild deviations from hydrostatic conditions; and t-4, when failure initiates (the red and purple line respectively; Fig. 3). For each model, the unknown V_p distribution within the slope is discretised to a stack of 36 cm-thick layers. In M-1, this totals 18 independent unknowns at t-2 and 52 at t-4. For each of the 50 independent GA runs, an initial population comprising 96 random p-wave models evolves for 120 generations. In M-2, the broader search range required a higher number

of models: at t-2, for 50 layers, 240 individuals and 120 generations; at t-4, for 82 layers, 480 individuals and 150 generations Stoffa & Sen (1991).

After FWI, the p-wave models are faithfully reconstructed. For each scenario, the median P-wave velocity model from 50 independent GA realisations is plotted in Figs. 5 and 6, and the inverted seismogram is compared to the synthetic field data. In M-1, at t-2 (Fig. 5b), the absence of reflections originating from the sediment column produces a smooth V_p model that contains only long-wavelength oscillations within the sediment column. At t-4 (Fig. 5e), the inversion identifies the depth of the acoustic anomaly associated with slope destabilisation at 14 m, and reconstructs effectively the characteristics of the true V_p profile. In M-2, although the mild porosity anomalies produce a less reflective acoustic profile, the inversion at t-2 (Fig. 6b) identifies the initiation of shallow overpressure build-up as a reduction of p-wave velocity at 7 m b.s.f.. At t-4 (Fig. 6e) the inversion scheme is capable of exploiting the weak negative-polarity reflections to retrieve correctly the main acoustic anomaly corresponding to slope failure at 20 m b.s.f

2.2.3 Estimation of effective stress conditions

In Figs. 7 and 8, φ_{est} for M-1 and M-2, respectively, are plotted against the true porosity profile, at times t-2 (panel a) and t-4 (panel d). In both scenarios, the true porosity profile has been reconstructed faithfully, with an accuracy reflecting the quality of the V_p solutions.

The optimal constants for the Eaton's and Bower's equations, which would in real cases be calibrated from in-situ soil measurements (e.g, Sayers, 2006), are here determined by a trial and error process. For Eaton's method, V_h is extrapolated from a portion of the solution V_p identified to be in nearly-hydrostatic conditions. Westbrook's method also required the the depth of the overpressured zone to be identified on the inverted V_p. These user-dependent parameters are

summarised in Table 2. The confidence intervals for λ^* and *FoS* shown in Figs. 7 and 8 result from applying the different techniques to the 95 % error boundaries of the seismic solution.

In M1, at t-2 (Fig. 7b-c), the long-wavelength noise of the V_p solution maps into a false broad overpressure anomaly, which, however, does not create a false destabilisation signature. At t-4 (Fig. 7e-f), the depth of the under-compaction anomaly is retrieved by each method: Eaton's successfully reconstructs λ^* and *FoS*, therefore identifying slope instability; Bowers' solution underestimates the amount of overpressure in the under-compacted zone, while overestimating it elsewhere; Westbrook's method approximates the overpressure profile, although it underestimates the maximum value. Stable and unstable conditions are successfully discriminated.

In M-2, at t-2 (Fig. 8b-c), Westbrook's method correctly quantifies the maximum λ^* value. Eaton's method fails, most probably as a result of an inaccurate extrapolation of the equilibrium baseline, whereas Bower's results shows the same limitations observed in M-1. Overall, the combination of methods yields a robust estimate of the in-situ effective stress conditions, detecting the presence overpressure within stability. At t-4 (Fig. 8e-f), the maximum value of λ^* is approximated by Eaton's method. Bower's solution, as in M-1, struggles to quantify overpressure changes; Westbrook's yields a less ambiguous result than Bower's, but underestimates the maximum λ^*. Also in this case, the combination of FWI and V_p–σ' transforms predicts failure within the confidence interval of the solution.

3 Discussion

3.1 Comments on overpressure estimation

In both case studies, the proposed two-step FWI-to–σ' approach allowed for the remote quantification of overpressure development, and the identification of slope destabilisation (Fig. 7

and 8). The final confidence intervals, for λ^* and *FoS*, result from combining the uncertainty of the inverted p-wave models to the inherent uncertainty associated with: a) the non-linear relationship between geophysical and geotechnical parameters; b) the choice of an appropriate relationship between p-wave velocity and in-situ effective stress.

The combined effect is that the ±5% uncertainty in the estimated V_p (Fig. 5 and 6) translates into a confidence interval for λ^* and *FoS* up to ±50% wide (Figs. 7 and 8), to which Bower's error boundaries are the major contributor. However, the inherently non-linear mapping between p-wave velocity and effective stress is such that even the method providing the less ambiguous estimates (Eaton's) produce λ^* boundaries ±30%-wide.

Among the methods tested, the true slope conditions at failure are best approximated by the Eaton (1975) approach, although, as shown in M-2 at t-2, it is liable to suffer from inaccuracies in the extrapolated equilibrium profile. The very high k_e exponent values ($\simeq$30, Tab. 2), however, indicate very low sensitivity. If the Eaton's relationship is re-written as $\sigma'=(\sigma_z-p_h)(\varphi_h/\varphi_{est})^{k_e}$, where we use porosity instead of V_p, the estimated k_e reduces to $\simeq$8 (Tab. 2). Therefore, the porosity formulation is in principle preferable, provided that the $Vp-\varphi$ relationship is reliable. The exponent obtained is higher than the values normally found in the literature Marin-Moreno et al. (2013), consistent with the high compressibility (low *E*') of the modelled shallow sediments (Tab. 1), in which great changes in porosity (driven by vertical deformation) can be brought about by little changes in effective stress.

The Bowers (1995) method performs reasonably within the under-compacted zones, but tends to overestimate overpressure elsewhere, and it's the main source of uncertainty in the estimated λ^*. This is possibly due to the assumed power law relationship between V_p and σ' not being adequate to represent the mapping between effective stress and *Vp* in the modelled shallow soft sediments.

The Westbrook (1991) technique yields reasonable, though generally underestimated, overpressure levels. Although it has the advantage of being independent of empirical constants, it requires an a-priori identification of the top of the overpressured zone on the inverted p-wave profile. This is a fairly univocal process in M-1 at t-4, but could be an important source of uncertainty in cases where such interface is difficult to locate, as in M-2.

The knowledge of a robust V_p−φ relationship is crucial for the estimation of bulk density and therefore the depth-dependent stress regime. Nevertheless, like other non-seismic information required in the proposed approach (grain, density, V_p−φ relationship, friction angle), a robust site-specific porosity transform can be obtained from measurements on few sampling site representative of the overall characteristics of the sediments in the survey area, which can then be quickly characterised with greater lateral resolution using seismic inversion.

3.2 Comments on stochastic FWI

Stochastic FWI has the advantage over local implementations (e.g., Virieux & Operto, 2009) of being robust to local minima entrapment when the knowledge of the true V_p model is poor (e.g., Aleardi et al., 2016). In addition to reducing the risk of obtaining misleading solutions, it allows an estimation of the solution repeatability, which here provides valuable information about the uncertainty associated to the remote determination of slope stability.

Remote characterisation using surface-acquired seismic reflection data provides a band-limited representation of the subsurface (Jannane, 1989; Virieux & Operto, 2009). This is apparent in a lack of sensitivity to the mid-to-long wavelengths components of the model, for example in the broad oscillation dominating the solution in M-1 at t-2. Such features do not produce significant traveltime changes in the given experimental setting, nor do they contain reflective interfaces, and therefore contaminate the reconstructed model without having an impact on its performance in the seismic model space. However, they can be mis-interpreted as

changes in-situ properties, and affect the pore pressure reconstruction (Fig. 7a-c). In new acquisition, these effects can be compensated for by employing broader source bandwidths and broader source-receiver offset range (Jannane, 1989); in legacy data, by using dedicated misfit functions and inversion strategies (e.g., Provenzano et al., 2018).

Stochastic FWI pays for the robustness and wealth of information with a high computing cost, as it requires computing a great number of synthetic seismograms (typically in the order of 10^5), as a function of the number of unknowns and the search range width (Tarantola, 2005). In this work, for each case study, 50 independent runs were spread across 5 high-performance computing nodes; each run took 8 hr on a 16-core 2.6 GHz node, for a total computing cost of about 3 days. GPU implementations of FWI are now gaining traction in the oil and gas community as a means to compress its computing cost (Yang et al., 2015), and are likely to be beneficial for the application of this methodology to engineering geology problems in the near future.

3.3 Summary of main sources of uncertainty

The proposed methodology is a two-step process involving the estimation of seismic velocity from full waveform reflection data, followed by the computation of excess pore pressure from the obtained seismic velocity (Fig. 2). The uncertainty on the final solution depends upon the intrinsic non-uniqueness of the seismic inversion, as well as on simplifying assumptions about the nature of the subsurface and the mapping from the geophysical to the geotechnical domain.

In the seismic characterisation step, the subsurface is approximated to an isotropically acoustic 1D layered medium. In real cases, the one-dimensional assumption can be approximated in subsurfaces with dipping layers by pre-stack time migrating the input seismic data (e.g., Mallick & Dutta, 2002). This parametrisation is limited in lateral resolution to the seismic imaging aperture, which is in the order of few tens of metres for UHF seismic reflection data

(Provenzano et al., 2017). However, the possibility to use of 2-3D inversion schemes is currently limited by the necessity to contain the number of unknowns of the stochastic optimisation (Tarantola, 2005). The acoustic assumption is sensible in this type of applications, since it is able to account for most of the energy of limited-offset reflection data acquired on young sediments with very low shear wave velocity (e.g., Provenzano et al., 2017).

In the geotechnical step, the calculated uncertainty arises from the very nature of the V_p-to- σ' relationship (Dugan & Sheahan, 2012), as made apparent by the application of different empirical transforms to the geophysical confidence intervals. The underlying assumption of most of such methods is that disequilibrium compaction is the only factor determining overpressure (Bowers, 1995). Although not valid in general (e.g., Marin-Moreno et al., 2012), this is sensible in young, shallow sediments (e.g., Sayers, 2006) where thermo-chemical and diagenetic effects are negligible.

A knowledge of the nature of the sediments under hydrostatic conditions is necessary for the remote characterisation of pore pressure anomalies, and it is dependent on the availability of in-situ measurements and core logs. This work suggests that the accuracy of the following input data is key to minimise the error in the estimation of the excess pore pressure:

- The availability of an appropriate relationship (e.g., Vardy, 2015) is necessary to obtain a reliable lithostatic stress and therefore excess pore pressure, as well as to apply Eaton's method to porosities.
- An accurate estimation of the equilibrium velocity profile is of paramount importance for a meaningful application of the Eaton method (Section 1.3). This can be obtained by performing a velocity inversion in a proximal site assumed to be in equilibrium and using the results as the baseline for the target site (e.g., Sayers et al., 2006).

- A sensible calibration of the empirical Bowers and Eaton constants (Tab. 2.) is also fundamental (Sayers et al., 2006), and it requires the use of control wells with in-situ pore pressure measurements.

As for the factor of safety, it is crucial to have reliable slope and friction angles. The impact of these parameters on the *FoS* estimate is highly non linear, as it depends, in a first approximation, from the ratio of their tangents (Eq. 3). The slope angle can be obtained from depth-converted migrated seismic section, whereas the friction angle can't be derived from seismic data, and should be measured on soil samples.

4 Conclusions

The main outcomes of this work can be summarised as follows:

- A well-parametrised stochastic full waveform inversion scheme reconstructs with high fidelity p-wave velocity reductions corresponding to disequilibrium compaction in the top 10 to 30 metres below seafloor.

- The obtained p-wave solution and confidence intervals can be mapped into porosity estimates whose accuracy and resolution reflects the quality of the p-wave inversion, and the reliability of the V_p-porosity relationship.

- In our models, the most accurate overpressure ratio estimates are obtained using the Eaton's method. Compared to basin scale applications, higher Eaton exponents are required for the very soft sediments of the shallow sub-seabed.

- An equivalent depth method is preferable where very shallow overpressure gradients prevent a reliable estimation of the equilibrium baseline, or where it's not possible to calibrate the Eaton's exponent.

- The overpressure ratio estimates are accurate enough to identify slope destabilisation during deposition, as well as quantify overpressure development within stability, in both synthetic slope models.

Within the limitation of the simple geotechnical model used, this work demonstrates that ultra-high frequency seismic reflection data can be used to characterise evolving effective stress conditions in shallow submarine slopes undergoing deposition. The time-effective data acquisition over large areas and the non-destructive nature of the methodology make this a promising tool for the integrated geophysical-geotechnical characterisation of landslide geohazard.

Acknowledgements

The seismic modelling was performed using the MIT OASES algorithm, and the data preconditioning used a combination of Seismic Unix and MatLab. All other processing and inversion used custom-written algorithms. The authors would like to thank Hector Marin Moreno for the advice regarding geomechanics. We acknowledge the use of the IRIDIS High Performance Computing Facility, and associated support services at the University of Southampton, in the completion of this work. Finally, we thank the Editor and the anonymous reviewers for the useful comments, which sensibly improved the quality of the manuscript

Funding

This research has been funded by the University of Southampton and the Engineering and Physical Science Research Council (EPSRC).

Table 1: **Model layer properties at deposition**. l_a= Low kinematic permeability bed. l_a=background sediments. *Rate* is the sedimentation rate, κ the kinematic permeability, ϱ_g the grain density, E'_0 the one-dimensional stiffness, φ the fractional porosity.

Table 2: **Constants for effective stress estimation**. Eaton's exponent, k_e calibrated either on porosity or on p-wave velocity. Bower's constants, *A* and *B*. Thickness of the inverted P-wave profile used to extrapolate the equilibrium curve, top_h. Minimum depth of overpressured portion for Westbrook's method, OP_{depth}. The latter is missing in M-1 at t-2 because no apparent deviation from equilibrium could be identified.

Figure 1: **Schematic slope model setup**. The figure represents the sedimentary sequences deposited for model M-1 and M-2, the position $D(t)$ of the sediment-water interface, and the bottom impermeable bedrock. The black curves represent, qualitatively, the permeability profiles for M-1 and M-2. Vertical axis, *z* is positive upwards, and Θ is the slope angle with respect to the horizontal.

Figure 2: **Summary of genetic algorithm FWI and effective stress estimation.** Multiple runs of genetic optimisation of the full waveform (GA-FWI) seismograms are used to obtain a robust estimate of the p-wave velocity distribution in the subsurface, and the confidence interval of the solution. The results of GA-FWI are then used to derive porosity, effective stress and therefore excess pore pressure within the slope.

Figure 3: **Evolution of geotechnical properties**: data for 4 timesteps during deposition, for M-1 (a-d) and M-2 (e-h), as a function of depth below the seafloor, labelled in *ka* (*kilo-annum*) after deposition starts. The relative bedrock position is shown as an horizontal dotted line with the same colour. The red dashed line in panels d and h is the FoS=1 line corresponding to slope failure.

Figure 4: **Seismic reflectivity evolution vs λ^***: seismic trace recorded at the nearest channel for the two case studies at the same time steps shown in Fig. 3. The maximum value of λ^* is reported in the legend, and a consistent colour palette is used. The seafloor and bedrock reflections evolution are followed by dashed lines, whereas the reflection associated with disequilibrium compaction is circled in red.

Figure 5: **Seismic data and model M-1**: Seismic data, and inversion results at t-2 and t-4. Seismograms (panels a, c, d, f) represented as amplitude density in greyscale. In panels b and d, the blue and grey shaded areas correspond respectively to the 66 and 95 % solution confidence intervals (σ here indicates standard deviation). Dashed lines connect reflected seismic phases in time-offset to the acoustic heterogeneity in depth.

Figure 6: **Seismic data and model M-2**: Seismic data, and inversion results at t-2 and t-4. Seismograms (panels a, c, d, f) represented as amplitude density in greyscale. In panels b and d, the blue and grey shaded areas correspond respectively to the 66 and 95 % solution confidence intervals (σ here indicates standard deviation). Dashed lines connect reflected seismic phases in time-offset to the acoustic heterogeneity in depth.

Figure 7: **Inverted geohazard properties M-1**. In panels (a, d) estimated porosity from median V_p solution and associated confidence intervals, respectively for t-2 and t-4. The dashed black line (EQ) indicates the extrapolated equilibrium compaction profile. In panels (b, e) overpressure ratios obtained by applying three different methods to the median and the 95% confidence interval V_p. Same in panels (c, f), for *FoS*. The dashed red line corresponds to *FoS*=1, i.e. instability.

Figure 8: **Inverted geohazard properties M-2**. In panels (a, d) estimated porosity from median V_p solution and associated confidence intervals, respectively for t-2 and t-4. The dashed black line (EQ) indicates the extrapolated equilibrium compaction profile. In panels (b, e) overpressure ratios obtained by applying three different methods to the median and the 95% confidence interval V_p. Same in panels (c, f), for *FoS*. The dashed red line corresponds to *FoS*=1, i.e. instability.

A Derivation of the governing equations

Assuming that water is incompressible, the net outflow of water from an infinitesimal layer within the model must equal the net volume loss due to deformation. If V is the volume of the layer at time t, we can write:

$$q_{out} - q_{in} = -\frac{\partial V}{\partial t} \tag{5}$$

By indicating the differential flux as dq and A as the area available for vertical flow:

$$dq = -A\frac{\partial u_z}{\partial t} \tag{6}$$

Therefore, since $\varepsilon_z = \frac{\partial u_z}{\partial z}$:

$$dq = A\frac{\partial \varepsilon_z}{\partial t}dz \tag{7}$$

Taking the differential of Darcy's law and combining with the above equation we arrive at the expression of mass balance:

$$\frac{\partial k}{\partial z}\frac{\partial h}{\partial z}+k\frac{\partial^2 h}{\partial z^2}=-\frac{\partial \varepsilon_z}{\partial t} \tag{8}$$

We assume that the material is linearly elastic with (constant) modulus E'_0:

$$\sigma'_z=E'_0\varepsilon_z \tag{9}$$

The constitutive expression, relating the stress rate to the strain rate, can be derived as:

$$\sigma'_z=\sigma'_z\left(\varepsilon_z(z,t)\right)$$

$$\frac{\partial \sigma'_z}{\partial t}=\frac{d\sigma'_z}{d\varepsilon_z}\frac{\partial \varepsilon_z}{\partial t}=E'_0\frac{\partial \varepsilon_z}{\partial t}$$

$$\frac{\partial \varepsilon_z}{\partial t}=\frac{1}{E'_0}\frac{\partial \sigma'_z}{\partial t} \tag{10}$$

The rate of change of the effective stress is:

$$\frac{\partial \sigma'_z}{\partial t}=\frac{\partial}{\partial t}\left(\sigma_z-p_h-p_e\right)=\frac{\partial}{\partial t}\left(\sigma_z-p_h-\gamma_w h\right)=\frac{\partial \sigma_z}{\partial t}-\frac{\partial p_h}{\partial t}-\gamma_w\frac{\partial h}{\partial t} \tag{11}$$

Taking into account that $\frac{\partial p_h}{\partial t}=0$ and combining with Eq. 10, the constitutive expression becomes:

$$\frac{\partial \varepsilon_z}{\partial t}=\frac{1}{E'_0}\left(\frac{\partial \sigma_z}{\partial t}-\gamma_w\frac{\partial h}{\partial t}\right) \tag{12}$$

Combining Eqs. 8 and 12 we obtain:

$$\frac{\partial k}{\partial z}\frac{\partial h}{\partial z}+k\frac{\partial^2 h}{\partial z^2}=-\frac{1}{E'_0}\left(\frac{\partial \sigma_z}{\partial t}-\gamma_w\frac{\partial h}{\partial t}\right) \tag{13}$$

Rearranging the terms we finally arrive at:

$$\frac{E'_0}{\gamma_w}\left(\frac{\partial k}{\partial z}\frac{\partial h}{\partial z}+k\frac{\partial^2 h}{\partial z^2}\right)+\frac{1}{\gamma_w}\frac{\partial \sigma_z}{\partial t}=\frac{\partial h}{\partial t} \qquad (14)$$

Assuming that the depth of submersion (d_0) remains constant, i.e. that sea level does not rise, the increase in total vertical stress σ_v over time at any given location z can only be due to deposition of new material. Deposition causes a uniform increase of σ_v through the depth of the layer, which in turn implies a uniform increase of the total stress normal to the slope (σ_z):

$$\frac{\partial \sigma_z}{\partial t} = \cos^2\Theta \frac{d\sigma_v}{dt} \qquad (15)$$

where the normal force increment is obtained as $dF_z=2l\cos\Theta d\sigma_v$ and then $d\sigma_z=dF_z\cos\Theta/(2l)$. Substituting the above into Eq. 14 yields the governing equation of the problem:

$$\frac{E'_0}{\gamma_w}\left(\frac{\partial k}{\partial z}\frac{\partial h}{\partial z}+k\frac{\partial^2 h}{\partial z^2}\right)+\frac{\cos^2\Theta}{\gamma_w}\frac{d\sigma_v}{dt}=\frac{\partial h}{\partial t} \qquad (16)$$

B Derivation of the moving top-boundary equation

Due to deposition, the thickness of the layer and therefore the location D of the top boundary, changes over time, i.e. $D=D(t)$. An additional equation to describe the velocity of this moving boundary is needed. The net upward movement of the boundary will be equal to the rate of deposition minus the rate of settlement due to consolidation:

$$\frac{dD}{dt}=\frac{1}{\gamma_s}\frac{d\sigma_v}{dt}+\left.\frac{\partial u_z}{\partial t}\right|_D \qquad (17)$$

where u_z is considered positive along the positive z-axis, i.e. for swelling rather than settlement. Swelling requires (downwards) flow into the soil of a fluid volume equal to that swept by the moving boundary. Considering an arbitrary area A on the slope surface, and using Eq. 7:

$$\left.\frac{\partial u_z}{\partial t}\right|_D A dt = -dq \cdot dt = k \left.\frac{\partial h}{\partial z}\right|_D A dt$$

$$\left.\frac{\partial u_z}{\partial t}\right|_D = k \left.\frac{\partial h}{\partial z}\right|_D \tag{18}$$

Combining Eqs. 17 and 18 we finally arrive at the governing equation for the moving boundary:

$$\frac{dD}{dt} = \frac{1}{\gamma_s}\frac{d\sigma_v}{dt} + k \left.\frac{\partial h}{\partial z}\right|_D \tag{19}$$

References

Aleardi, M., Tognarelli, A., & Mazzotti, A., 2016. Characterisation of shallow marine sediments using high-resolution velocity analysis and genetic-algorithm-driven 1d elastic full-waveform inversion, *Near Surface Geophysics*, **14**, 449–460.

Binh, N., Nakamura, T., Kozumi, K., Nakajima, M., Kubota, M., Kameya, H., & Taniue, M., 2009. Physical properties of the shallow sediments in late Pleistocene formations, Ursa Basin, Gulf of Mexico, and their implications for generation and preservation of shallow overpressures, *Marine and Petroleum Geology*, **26**, 474–486.

Bowers, G. L., 1995. Pore pressure estimation from velocity data: Accounting for pore pressure mechanisms besides undercompaction, *SPE Drilling and Completion*, **10**, 89–95.

Conway, K., Barrie, J., & Thomson, R. E., 2012. Submarine slope failures and tsunami hazard in coastal British Columbia: Douglas Channel and Kiti Mat arm, Tech. rep., Geological Survey of Canada.

Dey, A. & Lines, L. R., 1998. Seismic source wavelet estimation and the random reflectivity assumption, Research report 10, 21-1–21-28., CREWES.

Duarte, H., Wardell, N., & Monrigal, O., 2017. Advanced processing for UHR3D shallow marine seismic surveys, *Near Surface Geophysics*, **15**, 347–358.

Dugan, B. & Flemings, P., 2000. Overpressure and fluid flow in the new jersey continental slope: Implications for slope failure and cold seeps, *Science*, **289**, 288–290.

Dugan, B. & Sheahan, T., 2012. Offshore sediment overpressure of passive margins: mechanism, measurements, and models, *Reviews of Geophysics*, **50**.

Eaton, B. A., 1975. The equation for geopressure prediction from well logs, in *SPE 50th Annual Fall Meeting, SPE Paper 3544*, pp. 1–11.

Ferziger, J. & Perić, M., 2002. *Computational methods for fluid dynamics. 3rd edition*, Springer.

Flemings, P., Long, H., Dugan, B., Germaine, B., John, J., Behrmann, C., Sawyer, J., & expedition 308 scientists, I., 2008. Pore pressure penetrometers document high overpressure near the seafloor where multiple submarine landslides have occurred on the continental slope, offshore Louisiana, Gulf of Mexico., *Earth and Planetary Science Letters*, **269**, 309–325.

Garzaglia, S., Migeon, S., Ducassou, E., Loncke, L., & Mascle, J., 2005. Mass transport deposits on the Rosetta Province (NW nile deep sea turbidite system, Egyptian margin): characteristics, distribution, and potentiall causal processes., *Marine Geology*, **250**, 180–198.

Gibson, R., 1958. The progress of consolidation in a clay layer increasing in thickness with time, *Journal of Geophysical Research*, pp. 171–182.

Goldberg, D., 1989. *Genetic Algorithms in Search, Optimization, and Machine Learning*, Addison Wesley Publishing Company, Reading, MA.

Halflidason, H., Lien, R., Sejrup, H., Forsberg, H., & Bryn, P., 2005. The dating and morphometry of the Storegga Slide, *Marine and Petroleum Geology*, **22**, 123–136.

Huang, J. & Griffiths, V., 2010. One-dimensional consolidation theories for layered soil and coupled and uncoupled solutions by the finite-element method, *Geotechnique*, **60**, 709–713.

Jannane, M., 1989. Short note. Wavelength of earth structures that can be resolved from seismic reflection data, *Geophysics*, **54**(7), 906–910.

Lee, K. H. & Kim, H. J., 2003. Source-independent full waveform inversion of seismic data, *Geophysics*, **68**, 2010–2015.

Leynaud, D., Sultan, N., & Mienert, J., 2007. The role of sedimentation rate and permeability in the slope stability of the formerly glaciated Norwegian continental margin: the Storegga slide model, *Landslides*, **4**, 297–309.

L'Heureux, J.-S., Longva, O., Steiner, A., Hansen, L., Vardy, M. E., Vanneste, M., Haflidason, H., Brendryen, J., Kvalstad, T. J., Forsberg, C. F., Chand, S., & Kopf, A., 2012. Identification of weak layers and their role for the stability of slopes at Finneidfjord, northern Norway, *Submarine Mass Movements and Their Consequences. Advances in Natural and Technological Hazards Research*, **31**, 321–330.

Long, H., Flemings, P. B., Germaine, J. T., & Saffer, D. M., 2011. Consolidation and overpressure near the seafloor in the Ursa basin, deepwater Gulf of Mexico, *Earth and Planetary Science Letters*, **305**, 11–20.

Madhusudhan, B., Clare, M., Clayton, R., & Hunt, J., 2017. Geotechnical profiling of deep-ocean sediments at the AFEN submarine slide complex, *Quarterly Journal of Engineering Geology and Hydrogeology*.

Mallick, S. & Dutta, N., 2002. Shallow water flow prediction using prestack waveform inversion of conventional 3D seismic data and rock modeling, *The Leading Edge*, **21**, 675–680.

Marin-Moreno, H., Minshull, T., & Edwards, R., 2012. A disequilibrium compaction model constrained by seismic data and application to overpressure generation in the Eastern Black Sea Basin, *Basin Research*, **24**(1-17).

Marin-Moreno, H., Minshull, T., & Edwards, R., 2013. Inverse modelling and seismic data constraints on overpressure generation by disequilibrium compaction and aquathermal pressuring: application to the Eastern Black Sea Basin, *Geophysical Journal International*.

Masson, D. G., Harbitz, C. B., Wynn, R. B., Pedersen, G., & Løvholt, F., 2006. Submarine landslides: processes, triggers and hazard prediction, *Phil. Trans. R. Soc. A*, **364**, 2009–2039.

Mavko, G., Mukerji, T., & Dvorkin, J., 2009. *The rock physics handbook*, Cambridge U.P.

Menke, W., 1989. *Geophysical data analysis and inverse problems*, Academic Press INC.

Monrigal, O., Jong, I. D., & Duarte, H., 2017. An ultra-high-resolution 3D marine seismic system for detailed site investigation, *Near Surface Geophysics*, **15**, 335–345.

Pape, H., Clauser, C., & Iffland, J., 1999. Permeability prediction based on fractal pore-space, *Geophysics*, **64**, 1447–1460.

Pinson, L., 2009. *Derivation of Acoustic and Physical Properties from High-Resolution Seismic Reflection Data*, Thesis for the degree of doctor of philosophy, School of Ocean and Earth Sciences, University of Southampton.

Powrie, W., 2002. *Soil mechanics*, Spon, London.

Provenzano, G., Vardy, M., & Henstock, T. J., 2017. Pre-stack full waveform inversion of ultra-high-frequency marine seismic reflection data, *Geophysical journal international*, **209**, 1593–1611.

Provenzano, G., Vardy, M. E., & Henstock, T. J., 2018. Decimetric-resolution stochastic inversion of shallow marine seismic reflection data: dedicated strategy and application to a geohazard case study, *Geophysical Journal International*, **214**, 1683–1700.

Richardson, M. & Briggs, K., 1993. On the use of acoustic impedance values to determine sediment properties, in *Acoustic classification and mapping of the seabed*, vol. 15.

Sayers, C., 2006. An introduction to velocity-based pore-pressure estimation, *The Leading Edge*, pp. 1496–1500.

Sayers, C., Johnson, G., & Denyer, G., 2002. Predrill pore-pressure prediction using seismic data, *Geophysics*, **67**(4), 1286–1292.

Schmidt, H. & Jensen, F., 1985. A full wave solution for propagation in multilayered viscoelastic media with application to gaussian beam reflection at fluid-solid interfaces., *Journal of the Acoustic Society America*.

Sen, M. & Stoffa, P., 1996. Bayesian inference, Gibbs' sampler and uncertainty estimation in geophysical inversion, *Geophysical Prospecting*, **44**, 313–350.

Shanmugam, G., 2015. The landslide problem, *Journal of Palaeogeography*, **4**, 109–166.

Sheriff, R. & Geldart, L., 1995. *Exploration seismology*, Cambridge U.P., doi:10.1017/CBO9781139168359.

Skvortsov, A. & Bornhold, B., 2007. Numerical simulation of the landslide-generated tsunami in Kitimat Arm, British Columbia, Canada, 27 April 1975, *Journal of Geophysical Research*, **112**.

Steiner, A., L'Heureux, J.-S., Kopf, A., Vanneste, M., Longva, O., & Lange, M., 2012. *Submarine Mass Movements and Their Consequences*, chap. An In-Situ Free-Fall Piezocone Penetrometer for Characterizing Soft and Sensitive Clays at Finneidfjord (Northern Norway), Springer, Dordrecht.

Stigall, J. & Dugan, B., 2010. Overpressure and earthquake initiated slope failure in the Ursa region, northern Gulf of Mexico, *Journal of Geophysical Research*, **115**.

Stoffa, P. & Sen, M., 1991. Nonlinear multiparameter optimization using genetic algorithms: inversion of plane wave seismograms, *Geophysics*, **56**, 1794–1810.

Tarantola, A., 2005. *Inverse Problem Theory and Methods for Model Parameter Estimation*, ï¿¼ï¿¼Society for Industrial and Applied Mathematics.

Ulrych, T., 1971. Application of homomorphic deconvolution to seismology, *Geophysics*, **36**(4), 650–660.

Urlaub, M., Zervos, A., Talling, P., Masson, D., & Clayton, C., 2012. *Submarine mass movements and their consequences-How Do â¯¼2° Slopes Fail in Areas of Slow Sedimentation? A Sensitivity Study on the Influence of Accumulation Rate and Permeability on Submarine Slope Stability*, vol. 31 of **Advances in Natural and Technological Hazard Research**, Springer Netherlands.

Vanneste, M., Forsberg, C., Knudsen, S., Kvalstad, T., L'Heureux, J., Lunne, T., Vardy, M. E., Chand, S., Longva, O., Morgan, E., Kopf, A., Morz, T., Steiner, A., Brendryen, J., & Haflidason, H., 2015. Integration of very-high-resolution seismic and CPTU data from a coastal area affected by shallow landsliding - the Finneidfjord natural laboratory, *International Symposium on Frontiers in Offshore Geotechnics*, **3**.

Vardy, M., 2015. Deriving shallow-water sediment properties using post-stack acoustic impedance inversion, *Near Surface Geophysics*, **13**, 143–154.

Vardy, M., Vanneste, M., Henstock, T. J., Clare, M. A., Forsberg, C., & Provenzano, G., 2017. State-of-the-art remote characterization of shallow marine sediments: the road to a fully integrated solution, *Near Surface Geophysics*, **15**, 387–402.

Verbeek, N. & McGee, T. M., 1995. Characteristics of high-resolution marine reflection profiling sources, *Journal of Applied Geophysics*, **33**, 251–269.

Virieux, J. & Operto, S., 2009. An overview of full-waveform inversion in exploration geophysics., *Geophysics*, **74**(6).

Westbrook, G., 1991. Geophysical evidence for the role of fluids in accretionary wedge tectonics, *Phil. Trans. R. Soc. A*, **335**, 227–242.

Yang, P., Gao, J., & Wang, B., 2015. A graphics processing unit implementation of time-domain full-waveform inversion, *Geophysics*, **80**, F31–F39.

	Bed-type	Rate (mm/yr)	κ(m/s)	$\varrho_g (g/cm^3)$	E'_0 (kPa)	φ
M-1	l_b	3	10^{-6}	2.65	$0.5 \cdot 10^3$	0.7
	l_a	30	$3 \cdot 10^{-9}$	2.65	$0.5 \cdot 10^3$	0.7
	l_b	3	10^{-6}	2.65	$0.5 \cdot 10^3$	0.7
M-2	l_b	3	$1.6 \cdot 10^{-11}$ to $1.5 \cdot 10^{-9}$	2.65	10^3	0.6
	l_a	3	$1.6 \cdot 10^{-11}$	2.65	10^3	0.6
	l_b	3	$1.6 \cdot 10^{-11}$ to $7.0 \cdot 10^{-10}$	2.65	10^3	0.6
	l_a	3	$1.6 \cdot 10^{-11}$	2.65	10^3	0.6
	l_b	3	$1.6 \cdot 10^{-11}$ to $7.0 \cdot 10^{-10}$	2.65	10^3	0.6

Table 1: **Model layer properties at deposition**. l_a= Low kinematic permeability bed. l_a=background sediments. *Rate* is the sedimentation rate, κ the kinematic permeability, ϱ_g the grain density, E'_0 the one-dimensional stiffness, φ the fractional porosity.

	k_e (on φ_{est})	k_e (on Vp)	A	B	$top_h(m)$	OP_{depth} (m)
M-1, t-2	8	30	9.5	0.95	2	()
M-1, t-4	8	30	9.5	0.95	10	12
M-2, t-2	7	27	9.5	0.95	1	7
M-2, t-4	7	27	9.5	0.95	1	19

Table 2: **Constants for effective stress estimation**. Eaton's exponent, k_e calibrated either on porosity or on p-wave velocity. Bower's constants, A and B. Thickness of the inverted P-wave profile used to extrapolate the equilibrium curve, top_h. Minimum depth of overpressured portion for Westbrook's method, OP_{depth}. The latter is missing in M-1 at t-2 because no apparent deviation from equilibrium could be identified.

figure 1

Click here to access/download;figure;Figure1.png

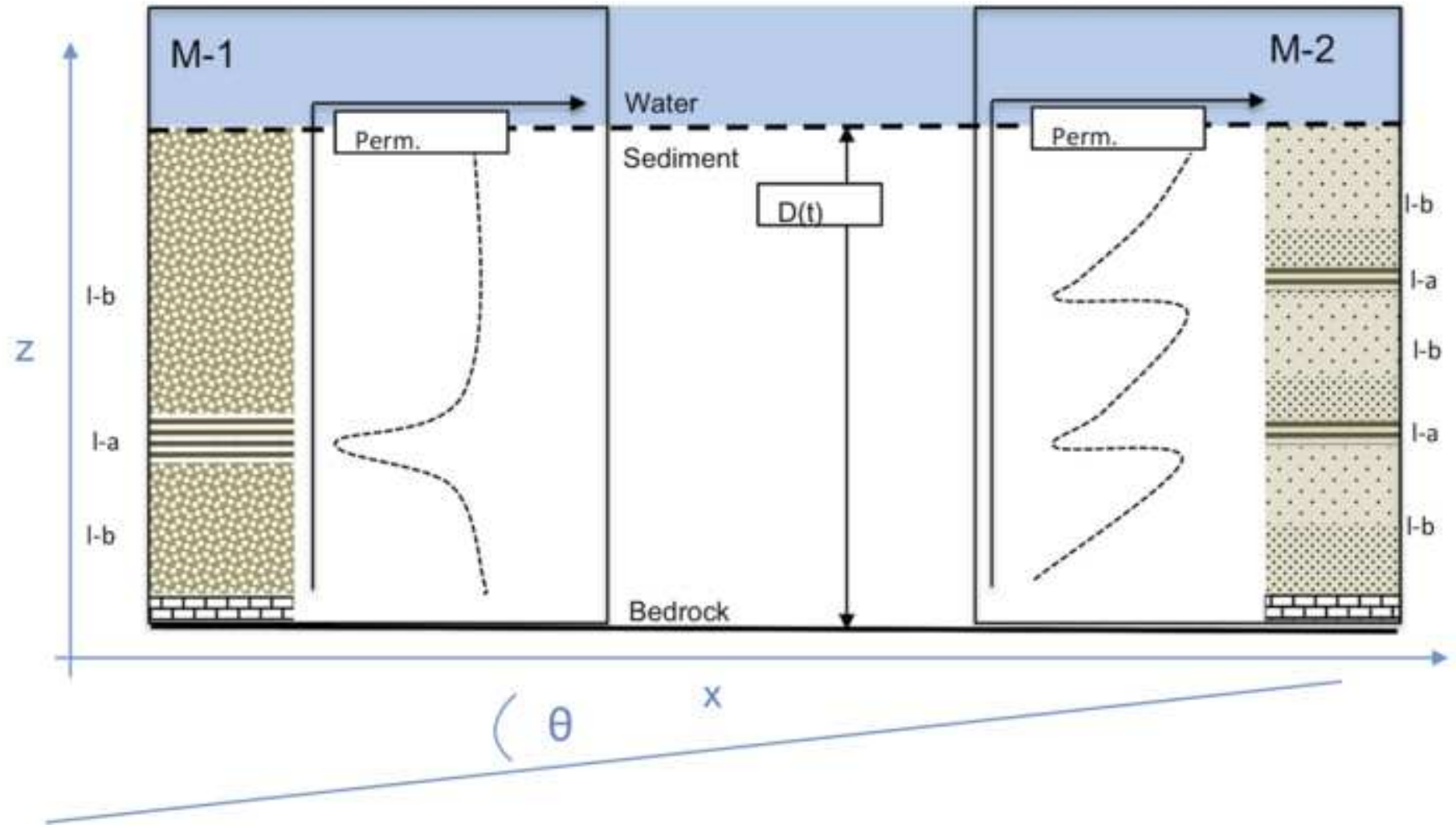

figure 2

Click here to access/download;figure;Figure2.png

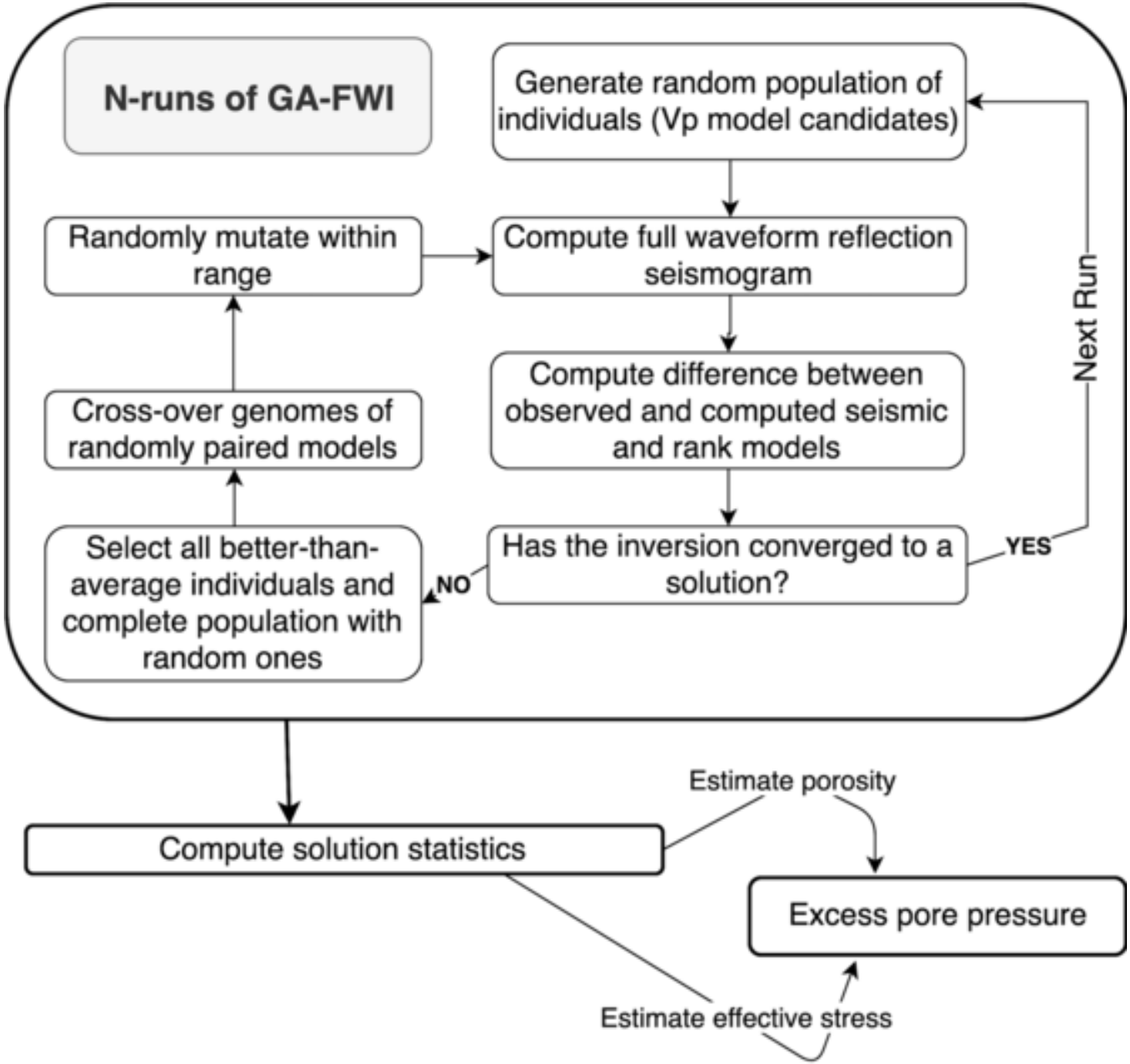

figure 3

Click here to access/download;figure;Figure3.png

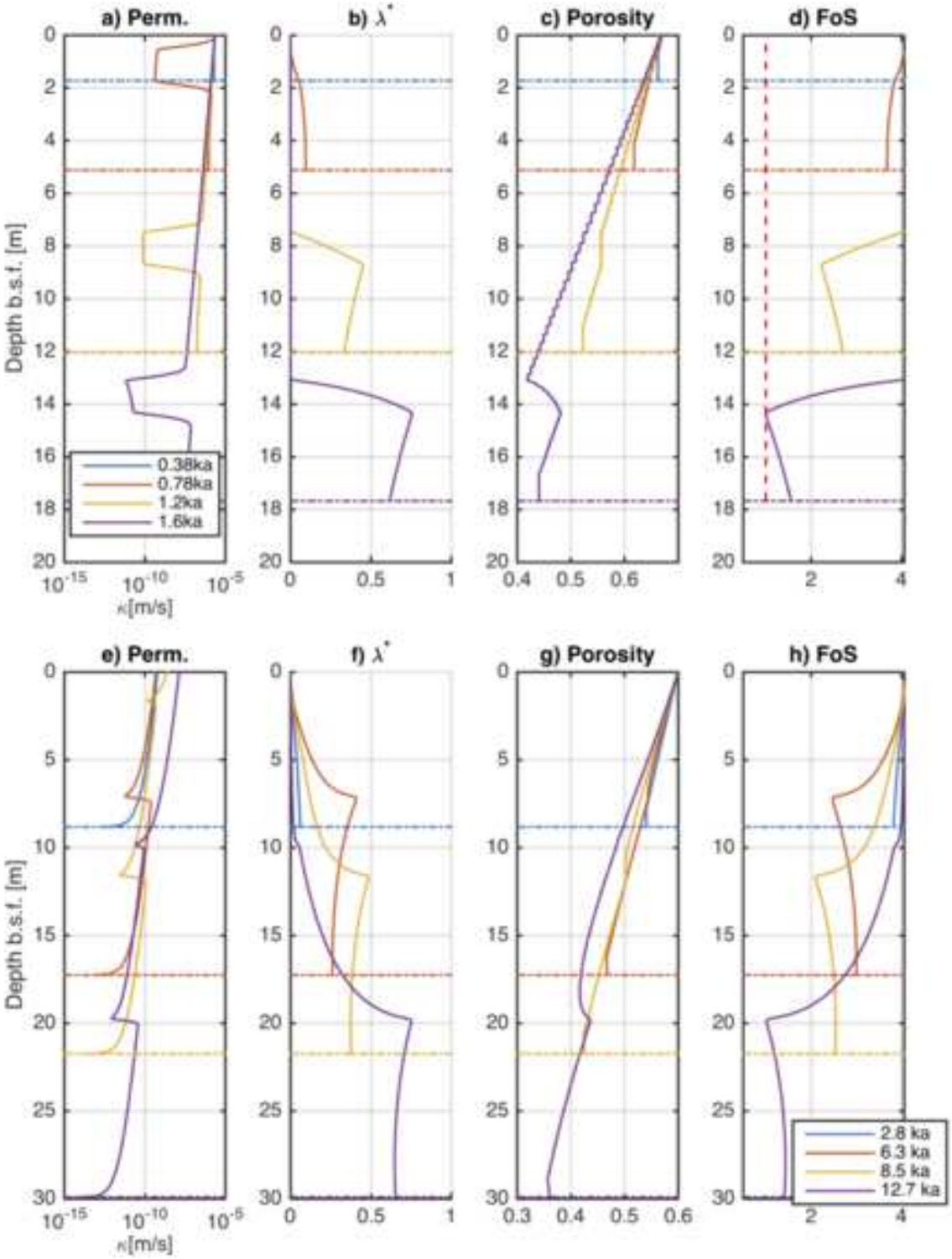

figure 4

Click here to access/download;figure;Figure4.png

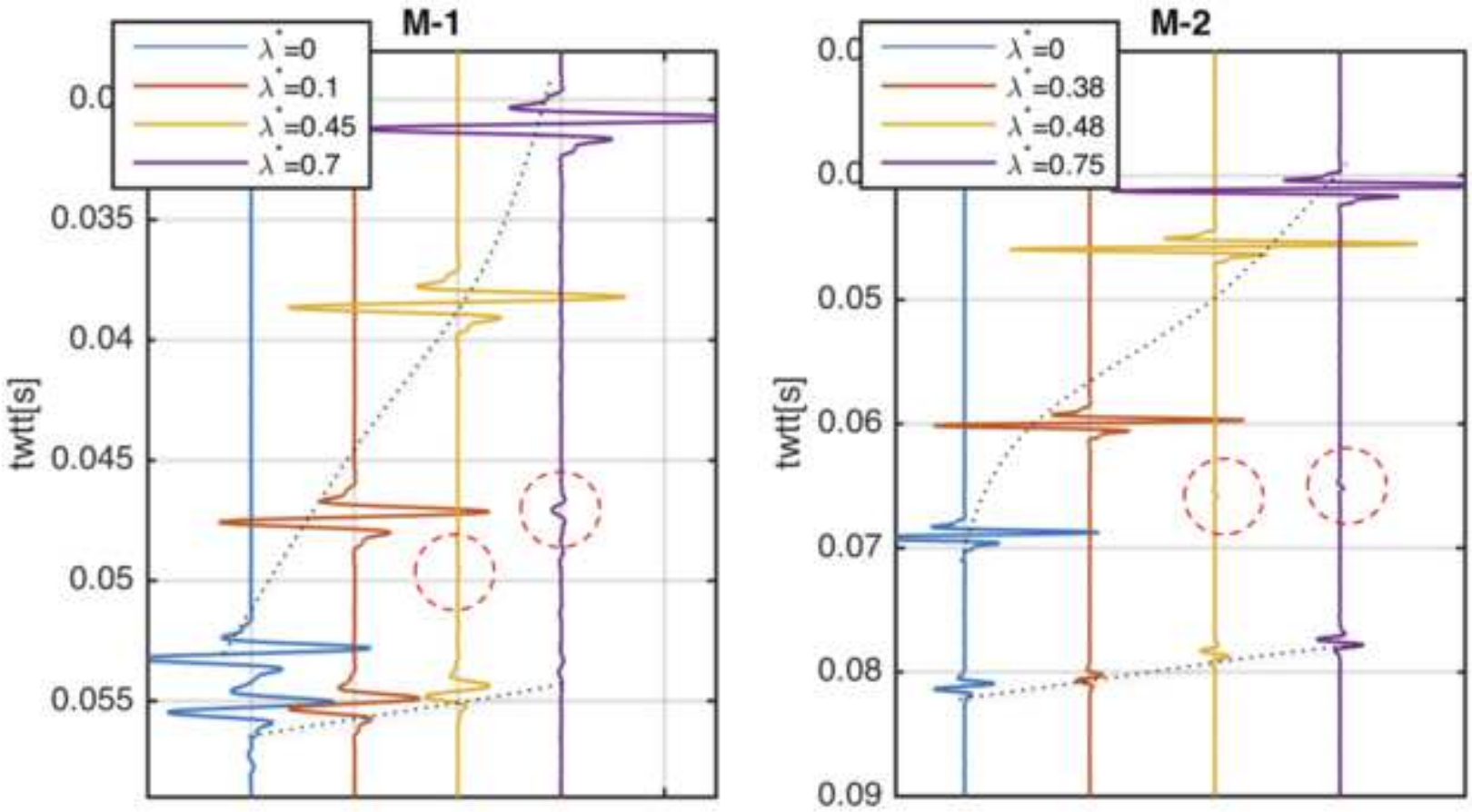

figure 5

Click here to access/download;figure;Figure5.png

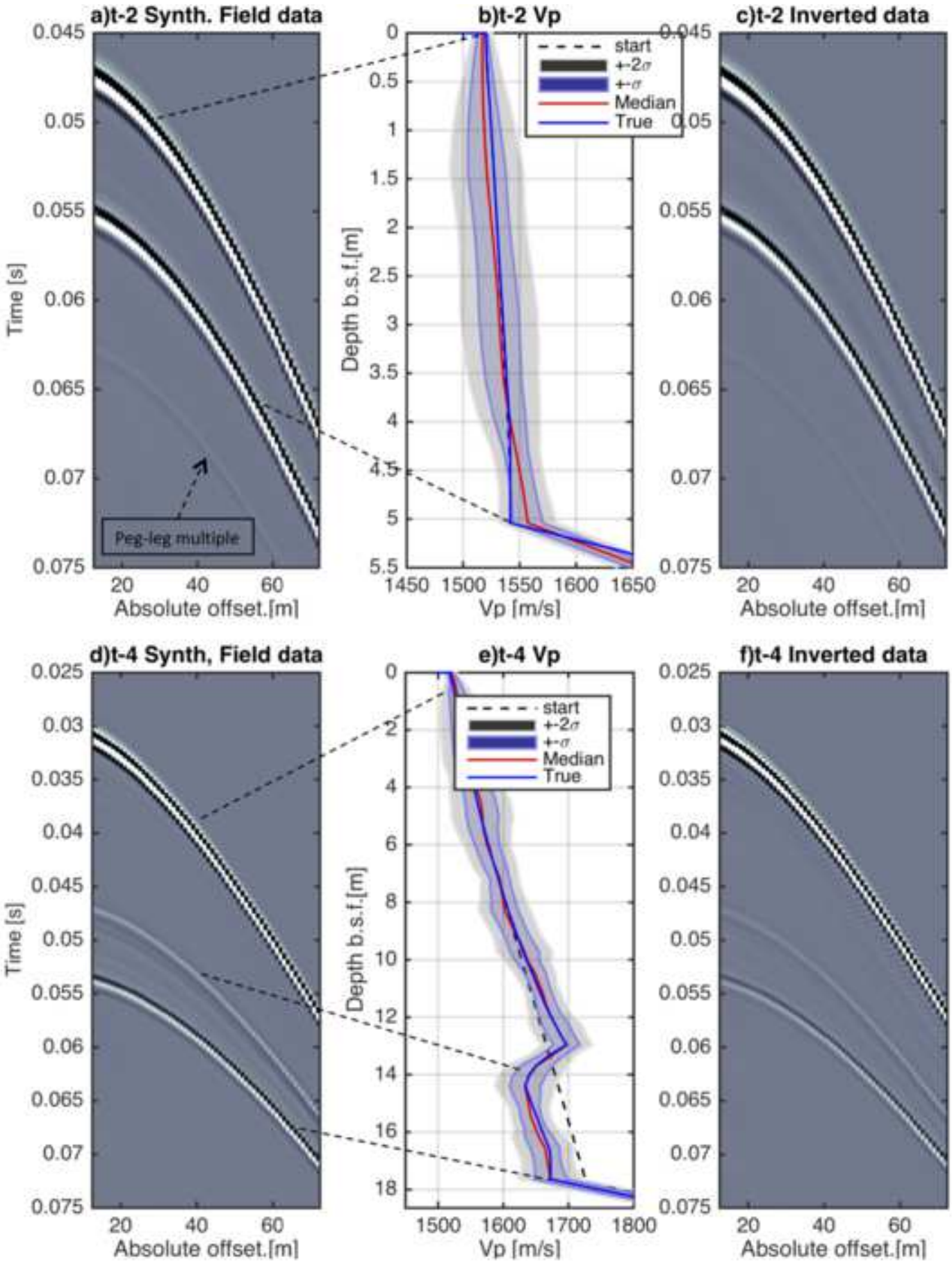

figure 6

Click here to access/download;figure;Figure6.png

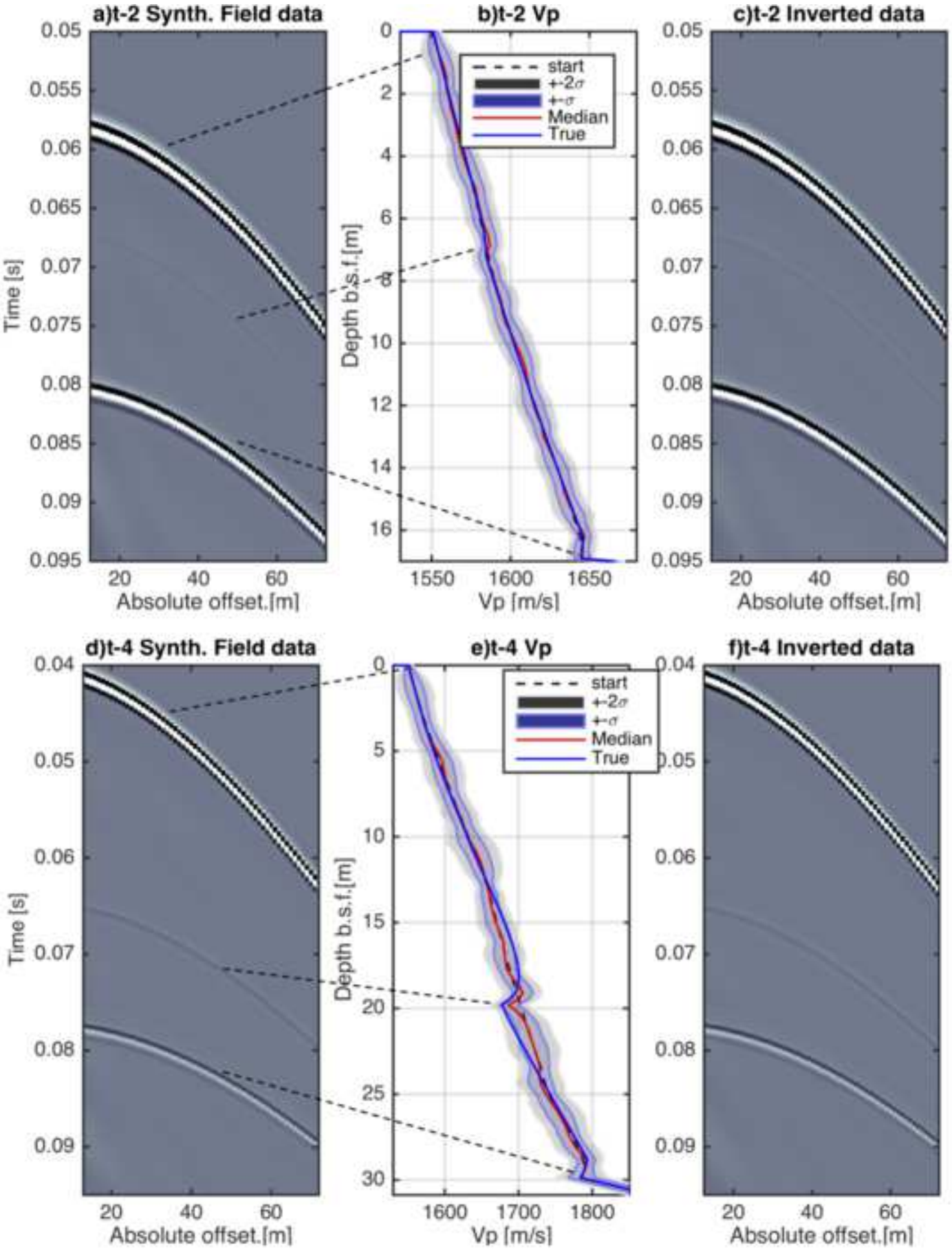

figure 7

Click here to access/download;figure;Figure7.png

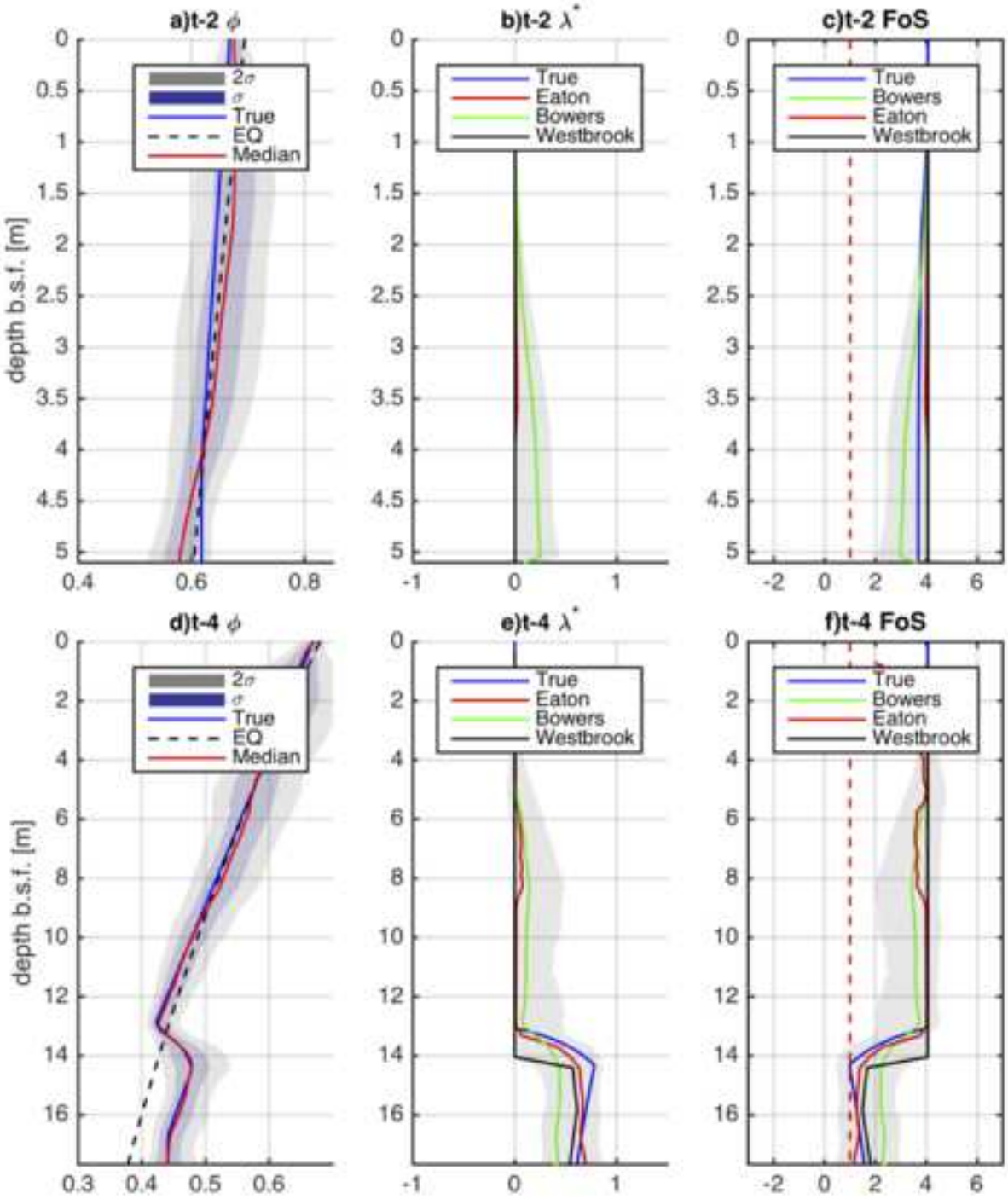

figure 8

Click here to access/download;figure;Figure8.png